Received: 12 April 2022 | Revised: 3 August 2022 | Accepted: 7 August 2022

DOI: 10.1002/aoc.6861

Applied Organometallic Chemistry WILEY

FULL PAPER

Preparation and evaluation of bismuth sulfide and magnetite-based theranostic nanohybrid as drug carrier and dual MRI/CT contrast agent

Hamed Nosrati[1] | **Marziyeh Salehiabar**[2] | **Faezeh Mozafari**[3] | **Jalil Charmi**[2] | **Nuri Erdoğan**[4] | **Mohammadreza Ghaffarlou**[5] | **Fatemeh Abhari**[3] | **Hossein Danafar**[3] | **Ali Ramazani**[1,6] | **Yavuz Nuri Ertas**[2,7]

[1]Department of Biotechnology, Research Institute of Modern Biological Techniques (RIMBT), University of Zanjan, Zanjan, Iran

[2]ERNAM—Nanotechnology Research and Application Center, Erciyes University, Kayseri, Turkey

[3]Zanjan Pharmaceutical Biotechnology Research Center, Zanjan University of Medical Sciences, Zanjan, Iran

[4]Department of Radiology, Erciyes University School of Medicine, Kayseri, Turkey

[5]Department of Chemistry, Hacettepe University, Ankara, Turkey

[6]Department of Chemistry, Faculty of Science, University of Zanjan, Zanjan, Iran

[7]Department of Biomedical Engineering, Erciyes University, Kayseri, Turkey

Correspondence
Ali Ramazani, Department of Biotechnology, Research Institute of Modern Biological Techniques (RIMBT), University of Zanjan, Zanjan, Iran.
Email: aliramazani@gmail.com; aliramazani@znu.ac.ir

Yavuz Nuri Ertas, ERNAM—Nanotechnology Research and Application Center, Erciyes University, Kayseri 38039, Turkey.
Email: yavuzertas@erciyes.edu.tr

Funding information
University of Zanjan; Iran's National Elites Foundation; Iran National Science Foundation, Grant/Award Number: INSF-98024375

Due to the increased incidence and population growth that has been leading to growing number of cases worldwide, early diagnosis and treatment of cancer is crucial. Low density cancer tissue cannot be diagnosed before progressing toward a metastatic stage. Thus, theranostic systems play a significant role in assisting timely diagnosis and treatment. The combination of magnetic resonance imaging (MRI) and computed tomography (CT) contrast agents in a single probe is of high importance and necessity, where individual strengths of each approach can be merged while shortcomings of each modality could be compensated. With this motivation, we have developed and synthesized Bi_2S_3@BSA-Fe_3O_4 nanoparticles as a dual MRI/CT contrast agent and carrier of curcumin (CUR) as natural anticancer drug. The nanoparticles shortened both the longitudinal (T_1) and transverse (T_2), MRI relaxation times, with a more distinct effect on producing negative contrast (T_2) images with a relaxivity (r_2) of 54.73 mM^{-1} s^{-1}. The magnetite/bismuth hybrid nanoparticle also was capable of increasing CT image contrast. Further, in vitro cytotoxicity assay showed high biocompatibility of the synthesized nanoparticles. Furthermore, in vitro cytotoxicity assay on cancer cells showed high anticancer activity of the synthesized nanoparticles.

KEYWORDS
bismuth, contrast agent, CT, iron oxide, MRI

1 | INTRODUCTION

Nanoscale systems allow for the early detection of illnesses as well as the monitoring of the therapeutic effects of nanoformulated medications in clinics. For simultaneous illness detection and therapy, several of innovative nanoparticles incorporate both drug(s) and imaging agent(s) within a single nanoparticle.

Magnetic resonance imaging (MRI) and computed tomography (CT) are traditional imaging techniques for evaluating extension, stage, and screening local tumors and distant metastases. However, efficacy of clinical approaches such as radiological imaging is questioned.[1] Imaging techniques can reveal tumor morphology and location clearly although they may be harmful to patients when contrast agents and high-energy radiations are used. CT provides poor spatial resolution and causes radiation damage while MRI has high sensitivity and specificity for diagnosing invasive breast cancer.[2] Despite the advantages of CT as a well-known imaging technique, major limitations such as low sensitivity in soft tissue remain to be a challenge.[3] Thus, MRI, a non-invasive imaging modality, is one of the preferred methods for screening breast cancer (BC), which is valuable for whole body imaging with high spatial resolution and sensitivity.[4] Another advantage of MRI is the higher contrast in soft tissues, contrary to CT.[5]

Conventional contrast agents used for CT imaging are accompanied by issues including non-specific nature, low sensitivity, and accumulation of toxic byproducts in renal system.[6] Therefore, the necessity of injecting large amount of contrast agents to acquire contrast-enhanced images is reported to be the main weakness of CT imaging, because contrast enhancement is based on the interaction between X-rays and heavy atoms, where suitable materials for this purpose have high atomic weights, and most of them are very toxic.[7] Minimizing the dose of heavy atoms while enhancing the CT image quality is of paramount importance. Current CT imaging technology requires the concentration of contrast agents to be in the millimolar range, while it is micromolar range for MRI.[8]

The resolution of MRI can be significantly improved by using contrast agents, which enhance the image contrast by shortening either the longitudinal (T_1) or transverse (T_2) relaxation times of water protons.[9] T_1 contrast agents shorten the T_1 time, which results in a positive/brighter image, while T_2 contrast agents reduce the T_2 time, producing negative/darker image. Contrast agents improve the rather low signal-to-noise ratio of normal tissues by selectively lowering the T_1 or T_2 relaxation times. Nowadays, ~35% of clinical MRI scans utilize contrast agents, but this is anticipated to grow as the next generation of multifunctional MRI contrast agents become more widely available.[10] The performance of a contrast agent is assessed by its r_1 ($1/T_1$) or r_2 ($1/T_2$) relaxivity (the relaxation enhancement of solvent water protons at a concentration of 1 mM) as well as the r_2/r_1 ratio. As the r_2/r_1 ratio increases, the substance becomes a more efficient T_2 contrast agent and a less efficient T_1 contrast agent, and vice versa.[11]

Magnetic nanoparticles play important roles in tumor treatment, drug delivery, and particularly as MRI contrast agents due to their magnetic response upon application of an external magnetic field.[12,13] Iron oxide nanoparticles are biocompatible, biodegradable, have long blood circulation time, and they have effective clearance from body (degradation to hemoglobin naturally).[14,15] These nanoparticles have been extensively investigated as a T_2 contrast agent as they shorten transverse relaxation time.[16] Several formulations of iron oxide nanoparticles received FDA approval as T_2 contrast agents, while many of them were withdrawn from market.[17,18] Furthermore, through the adjustment of size, shape, and surface groups, both T_1 and T_2 relaxations can be enhanced in a single iron oxide nanoparticle.[19]

In order to improve the sensitivity and accuracy of breast cancer diagnosis, the combination of CT and MRI in a single probe is of paramount importance and necessity, where individual strengths of each approach can be merged while shortcomings of each modality could be compensated. High atomic number-based nanoparticles, which increase X-ray attenuation, are applied for precise tumor detection in CT imaging. Bismuth nanoparticles show excellent CT imaging effect due to bismuth having a large atomic number ($Z = 83$), high X-ray attenuation coefficient, and biocompatibility.[20,21] Unlike other elements with high atomic number, bismuth can be easily oxidized and solubilize in physiological environment and excreted from body in ionized form.[22] Dual mode contrast agent ultrasmall nanoparticles consisting of bismuth and gadolinium were employed to enhance the image contrast to locate tumor site accurately, and in vivo CT/MRI contrast enhancement was demonstrated in a non-small cell lung carcinoma model.[23] Here, gadolinium atoms provided the T_1 MRI contrast, while gadolinium and bismuth atoms together contributed to CT imaging contrast. In another study, Bi_2Se_3 nanoplates coated with poly (vinylpyrolidone) (PVP) were produced to explore their potential in CT imaging and cancer radiation therapy. It was shown that accumulation of Bi in the tumor cells increased through the enhanced permeability and retention (EPR) effect, and the growth of the cancer cells were largely inhibited upon application of radiotherapy.[24] In order to increase the solubility and receptor-mediated cancer

cell targeting, Bi_2O_3 nanoparticles were functionalized with hyaluronic acid. Hyaluronic acid conferred the nanoparticles specific targeting of cancer cells overexpressing CD 44 receptors, and tumor-targeted CT contrast enhancement was observed.[25] Elsewhere, anticancer drug loaded mesoporous silica-coated bismuth sulfide nanoparticles were developed toward targeting and treatment of osteosarcoma, where bismuth was utilized for both photothermal effect and real-time CT monitoring. The nanoparticles showed distinct CT contrast at the tumor site, producing higher effect than the clinically used agent.[21] There are a couple of studies have used BSA for coating of NPs.[26–28] BSA also have extensively used for biomineralization synthesis process of NPs.[29,30] Although CT and MRI have different advantages and limitations, contrast agents that have the potential to utilize the superiorities of each imaging modality are of great interest. Considering the toxicity of gadolinium-based materials, safe alternatives are desired, and recent research in MRI contrast agent field has been centered around the iron oxide nanoparticles, especially after it was confirmed that they can function as effective T_1 contrast agents.[31,32] Because the biocompatibility and CT contrast enhancement effect of bismuth is well documented, here, we report eco-friendly synthesis of Bi_2S_3 and Fe_3O_4 in a single nanoparticle stabilized with bovine serum albumin (BSA). Synthesized nanoparticles not only served as dual mode CT/MRI contrast agent but also used as carrier of curcumin anticancer drug.

2 | METHODS AND MATERIALS

2.1 | Materials

$Bi_2(NO_3)_3.5H_2O$, BSA, and CUR were purchased from Sigma-Aldrich. $FeCl_2.4H_2O$, $FeCl_3.6H_2O$, and NH_4OH were purchased from Merck.

2.2 | Synthesis of bismuth sulfide nanoparticles and surface modification with BSA

The 50 mM $Bi_2(NO_3)_3$ was added to 1 ml of 2 M nitric acid, and the mixture was added to 8 ml of BSA solution (31.25 mg ml^{-1}) gradually while stirring vigorously. Bi_2S_3@BSA was formed after bio-mineralization process[33] by the addition of NaOH solution to Bi-BSA complex and stirring for 12 h. To purify Bi_2S_3@BSA nanoparticles, they were dialyzed for 48 h against distilled water and stored at 4°C.

2.3 | Synthesis of magnetite/bismuth hybrid nanoparticles (Bi_2S_3@BSA-Fe_3O_4)

NH_4OH was added drop-wisely to a vigorously stirring solution containing $FeCl_2.4H_2O$ (40.0 mg), $FeCl_3.6H_2O$ (110.0 mg), and Bi_2S_3@BSA nanoparticles in N_2 atmosphere with the temperature adjusted to 60°C. So, Fe_3O_4 nanoparticles were produced in the presence of Bi_2S_3@BSA nanoparticles and the product, Bi_2S_3@BSA-Fe_3O_4, was dialyzed against distilled water for 48 h.

2.4 | Synthesis of CUR loaded Bi_2S_3@BSA-Fe_3O_4 (Bi_2S_3@BSA-Fe_3O_4@CUR)

The 30 mg aqueous solution of Bi_2S_3@BSA-Fe_3O_4 (3 ml) was simply mixed with 10 mg of CUR in 2 ml ethanol. The solution stirred in a round bottom flask without bung for 24 h under the dark condition at room temperature. After evaporating ethanol, unloaded CUR was precipitated via centrifugation at 8000 rpm three time.

2.5 | Characterization of as-synthetized hybrid nanostructure

Scanning transmission electron microscopy (STEM, Vega Tescan) was used to characterize the morphology and structure of as-prepared Bi_2S_3@BSA and Bi_2S_3@BSA-Fe_3O_4. Optical properties of nanoparticles were characterized by UV–Vis spectroscopy (PG Instruments, T80).

Energy-dispersive X-ray spectroscopy (EDS, Supra 35VP Leo EDS instrument) and X-ray powder diffraction (XRD, Bruker AXS model D8 Advance diffractometer) were employed for elemental analysis of the end product. Mean hydrodynamic particle size and size distribution of nanoparticles were determined by Nano/Zeta Sizer (Malvern Instruments, Worcestershire, UK, ZEN 3600 model Nano ZS) using dynamic light scattering (DLS).

2.6 | Drug content amount

The 1 mg of Bi_2S_3@BSA-Fe_3O_4@CUR was dispersed in 1 ml ethanol to measure the CUR content of produced nanoparticles. The solution was centrifuged after 2 h of shaking, and the absorbance of the supernatant, which included CUR, was measured at 428 nm with a UV–Vis spectrophotometer (T80 double beam spectrophotometer, PG Instruments Limited). With the help of the CUR standard curve, the quantity of released CUR was computed. Finally, using Equation (1), the drug loading was computed.

$$\%Drug\ Loading\ (DL) = \frac{Loaded\ Drug\ (mg)}{\text{Drug loaded carrier (mg)}} = \frac{Loaded\ CUR\ (mg)}{\text{CBNPs@BSA} - \text{CUR (mg)}} \quad (1)$$

2.7 | Drug release study

The release of CUR was studied at two distinct pH: pH 4 and pH 7.4. Briefly, 1 mg of Bi_2S_3@BSA-Fe_3O_4@CUR were dispersed in 500 µl PBS:ethanol (65:35), then placed into a dialysis bag to assess the CUR release profile. The dialysis bag was then submerged in 35.0 ml of a PBS:ethanol (65:35) containing container and agitated at 100 rpm and 37°C. At predetermined time intervals, 1 ml of dialyzed solution was removed and returned to the container, after reading the absorbance at 428 nm using a UV–Vis spectrophotometer.

2.8 | Cytotoxicity studies

MTT assay was performed on human umbilical vein endothelial cells (HUVEC) and 4T1 breast cancer cell line to determine the cytotoxicity and anticancer ability of nanoparticles. The cells were cultured in RPMI-1640 medium containing 10% fetal bovine serum (FBS) and 1% antibiotics (penicillin streptomycin, 10,000 U ml^{-1}) at 37°C, saturated humidity and 5% CO_2.

The cytotoxicity of Bi_2S_3@BSA-Fe_3O_4 and Bi_2S_3@BSA-Fe_3O_4@CUR on cells were assessed by MTT cell viability assay. The cells were seeded in 96-well plates with a density of 5×10^3 cells/well for 24 h. The medium was replaced with 100 µl of the medium containing different concentrations of nanoparticles. The cells were co-incubated with nanoparticles for 24 h. Incubation continued for 4 h after adding 20 µl of MTT solution (5 mg ml^{-1}). Following the removal of the growth medium, produced formazan was dissolved in 100 µl of dimethylsulfoxide (DMSO). Then, the absorbance of each well was measured at 570/640 nm via a microplate reader (SpectraMax M2 Microplate reader, Molecular Devices). Cell viability was calculated based on the control group.

2.9 | In vitro MRI imaging

Suspensions of Bi_2S_3@BSA-Fe_3O_4 nanoparticles were prepared, and the medium was diluted systematically. Diluted mediums over a range of concentrations in 12-well plate were placed vertically within the head coil at room temperature. MRI was performed using clinical 3T whole body magnetic resonance scanner (Siemens Avanto Medical Systems). Inversion recovery sequence was used to measure the longitudinal relaxivity (r_1), where TI (inversion time), TR (repetition time) and TE (echo time) were set as follows:

$$TI = (100, 200, 500, 1000, 1700, 2500)\ ms; TR = 3000\ ms; TE = 15\ ms$$

Multi-echo spin-echo sequence was used to measure the transverse relaxivity (r_2),where TR was fixed in 2000 ms and TE was set at (40, 60, 80, 100, 150, and 250) ms. In addition to one blank phantom, six phantoms containing six different concentrations (0.97, 0.49, 0.24, 0.12, 0.015, and 0.0076 mM) of nano contrast agent were prepared.

For both sequence modes, slice thickness (3 mm), field of view (FOV, 74 * 149 mm), and matrix size (420 * 335 pixel) values were kept same, and MRI phantoms were prepared (T_2-weighted and T_1-weighted), then analyzed. As described in Alipour et al.,[34] signal intensities at all TI values were gathered within a region of interest (ROI) and T_1 relaxation time was calculated via Levenberg–Marquardt method to solve the nonlinear equation, and similarly, T_2 values at all TE values were calculated. Following T_1 and T_2 calculations, relaxation rates (R_1 and R_2) were estimated and eventually r_1 and r_2 were quantified.

2.10 | In vitro CT imaging

To evaluate the potential application of Bi_2S_3@BSA-Fe_3O_4 nanoparticles as CT contrast agent, phantoms composed of different concentrations of nanoparticles (based on Bi, mM) were prepared in 2 ml vials. CT phantoms were prepared using Toshiba Aquilion LB (Model TSX-210A) CT scanner. FOV (373 mm), image matrix (512 * 512), and slice thickness (5 mm) were fixed and X-ray voltage (80 kV) and anode current (23 mA) were set. Images were analyzed on the basis of signal intensity by employing Macro Imaging software.

3 | RESULTS AND DISCUSSION

3.1 | Synthesis of nanohybrid Bi_2S_3@BSA-Fe_3O_4

The synthesis of the Bi_2S_3@BSA-Fe_3O_4 nanoparticles involved three separate steps (Figure 1). (I) Preparation of Bi_2S_3@BSA: In this step, Bi_2S_3@BSA nanoparticles

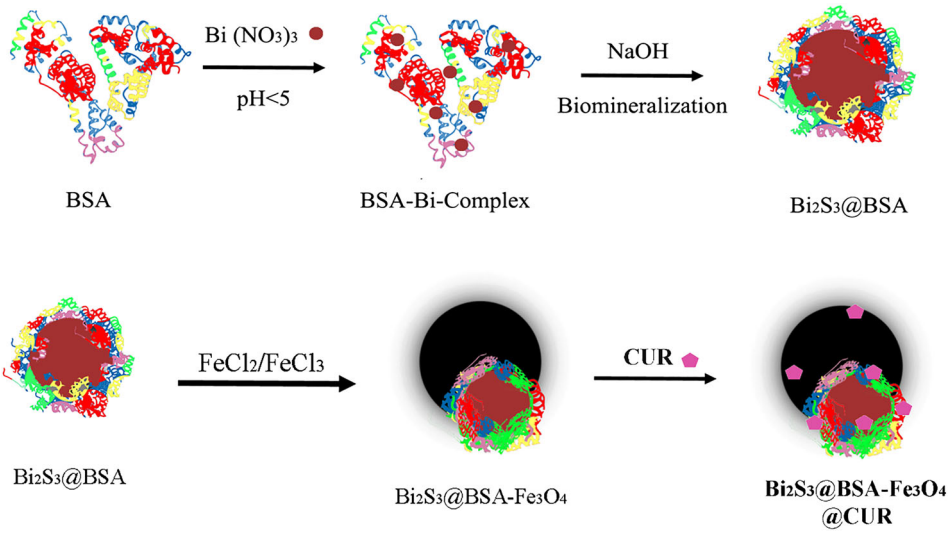

FIGURE 1 Schematic illustration of the synthesis steps of CUR loaded magnetite/bismuth sulfide nanohybrid.

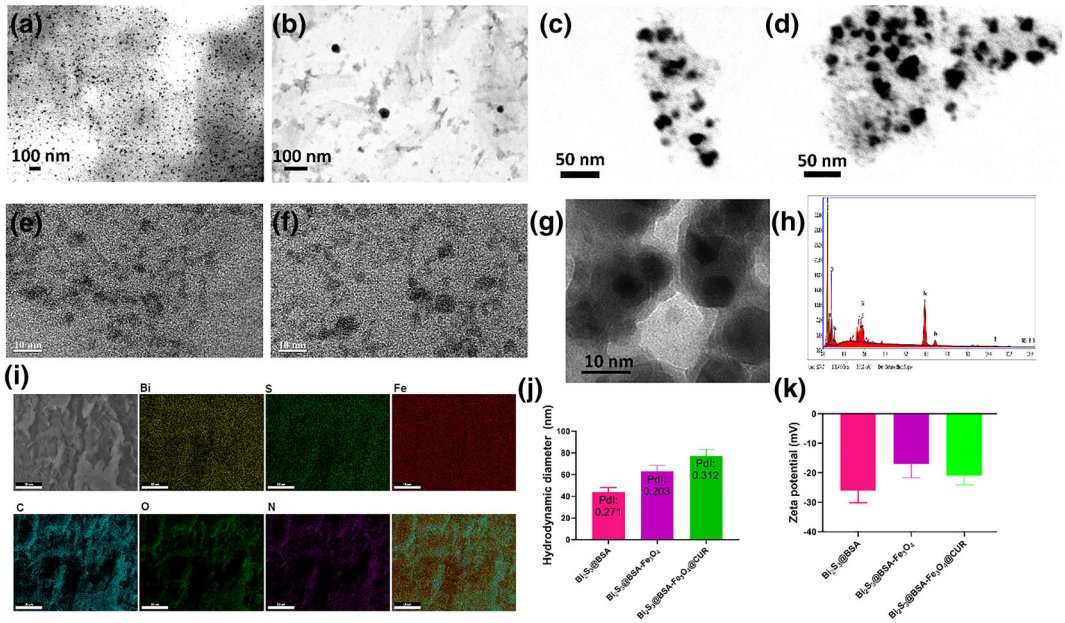

FIGURE 2 STEM images of (a) Bi_2S_3@BSA, (b, c) Bi_2S_3@BSA-Fe_3O_4; and (d) Bi_2S_3@BSA-Fe_3O_4@CUR; (e) TEM image of Bi_2S_3@BSA-Fe_3O_4; (f) TEM image of Bi_2S_3@BSA-Fe_3O_4@CUR; (g) TEM image of Bi_2S_3@BSA-Fe_3O_4; (h) SEM-EDS elemental mapping; (i) EDS spectrum analysis, (j) Hydrodynamic size of Bi_2S_3@BSA, Bi_2S_3@BSA-Fe_3O_4, and Bi_2S_3@BSA-Fe_3O_4@CUR; (k) Zeta potential of Bi_2S_3@BSA, Bi_2S_3@BSA-Fe_3O_4, and Bi_2S_3@BSA-Fe_3O_4@CUR

were prepared using biomineralization of BSA in the presence of Bi $(NO_3)_3$ and NaOH. Here, BSA plays two main roles simultaneously: (1) as a major sulfur source for the preparation of Bi_2S_3 and (2) as a coating agent for stabilizing the nanoparticles.[33] NaOH was used for denaturation and biomineralization of the BSA.[33,35] (II) Preparation of the magnetite/bismuth hybrid nanoparticle, Bi_2S_3@BSA-Fe_3O_4: In this step, Fe_3O_4 nanoparticles were synthesized via co-precipitation method in the presence of pre-synthesized Bi_2S_3@BSA nanoparticles. Nano sized magnetite was synthesized to form the magnetite/bismuth hybrid nanoparticle, Bi_2S_3@BSA-Fe_3O_4. (III) Preparation of CUR loaded the magnetite/bismuth hybrid nanoparticle, CUR was loaded onto Bi_2S_3@BSA-Fe_3O_4 nanoparticles via simple mixing method. Because the Bi_2S_3@BSA-Fe_3O_4@CUR nanoparticles did not precipitate via centrifugation, in this method we precipitated unloaded CUR via centrifugation.

3.2 | Characterization

Morphology, size, structure, and composition of prepared nanohybrid particles were elucidated by using several characterizing techniques.

STEM and TEM techniques were employed to determine shape and size of the nanoparticles. It is evident that the size of Bi_2S_3@BSA nanoparticles (Figure 2a) increases after the incorporation of Fe_3O_4 into the nanostructure (Figure 2b,c). The synthetized nanoparticles (Bi_2S_3@BSA-Fe_3O_4) were monodisperse and semi-spherical in shape (Figure 2b,c), which is also evident in the representative TEM image (Figure 2e). STEM and TEM images show that CUR loaded nanoparticles (Bi_2S_3@BSA-Fe_3O_4@CUR) have spherical shape (Figure 2d,f). Bismusth has a higher electron density than iron, so Bi_2S_3 appears darker than Fe_3O_4 in TEM images (Figure 2g).

Elemental distributions and composition of Bi_2S_3@BSA-Fe_3O_4 were further investigated by employing elemental analyses. Energy dispersive X-ray point spectroscopy (EDS) confirmed the existence of C, O, Fe, and Bi elements in the final synthetized material, Bi_2S_3@BSA-Fe_3O_4 (Figure 2h). The peaks for C, N, and O refer to the presence of BSA on the surface of nanoparticles. Characteristic peaks of Fe, Bi, S, and O indicate the successful synthesis of magnetite/bismuth nanohybrid. Elemental maps demonstrated even distribution of Bi, Fe, and S across the sample, uniform distribution, confirming the formation of dual hybrid structure (Figure 2i).

To investigate the hydrodynamic size and surface charge of nanoparticles, dynamic light scattering (DLS) technique was employed. Mean nanoparticle size and polydispersity index (PDI) are represented in Figure 2j. Based on the DLS measurements, Bi_2S_3@BSA, Bi_2S_3@BSA-Fe_3O_4, and Bi_2S_3@BSA-Fe_3O_4@CUR have an average diameter of 44 nm, 63 nm, and 77 nm, also a narrow particle size distribution with a PDI of 0.271, 0.203, and 0.312, respectively. Zeta potential is a key parameter for the stability of nanoparticles and cell-nanoparticle interactions. Noting that plasma and blood cells possess negative surface charge, negatively charged nanoparticles display poor electrostatic interaction, thus circulate longer in the blood stream. As shown in Figure 2k, mean zeta potential of Bi_2S_3@BSA, Bi_2S_3@BSA-Fe_3O_4, and Bi_2S_3@BSA-Fe_3O_4@CUR were found to be −26 mV, −27 mV, and −21 mV, respectively, which is considered ideal for in vitro studies and biological applications. The negative charge mainly arises from the existence of Fe, Bi, and BSA in the structure of the nanoparticle.

UV–Vis spectrophotometer was used to confirm the successful synthesis of the final product. UV–Vis spectra of iron oxide (Fe_3O_4), CUR, Bi_2S_3@BSA, Bi_2S_3@BSA-Fe_3O_4, and Bi_2S_3@BSA-Fe_3O_4@CUR nanoparticles are shown in Figure 3a. The Fe_3O_4 nanoparticles (IONPs) do not display a characteristic peak, whereas discernible absorption is observed in the spectrum of Bi_2S_3@BSA nanoparticles at 265 nm, which indicates the coating of BSA.[36] The same peak appeared at a higher wavelength for Bi_2S_3@BSA-Fe_3O_4, indicating the interaction of Fe_3O_4 with Bi_2S_3@BSA in the final structure. CUR shows a broad peak at 428 nm. Bi_2S_3@BSA-Fe_3O_4@CUR nanoparticles not only show Bi_2S_3@BSA-Fe_3O_4 peak at 272 nm, but also absorbance of CUR was shown at 422 nm, which verified loading of CUR onto nanoparticles.

XRD is another useful tool for the analysis of newly synthetized compounds, and it was used to characterize the chemical composition and crystallinity of the nanoparticles. Crystalline structure identification was employed to verify the structure of Bi_2S_3@BSA-Fe_3O_4. Figure 3b presents the diffraction pattern of Bi_2S_3@BSA-Fe_3O_4, and this was compared with standard X-ray patterns of Bi_2S_3 and Fe_3O_4. XRD pattern of Bi_2S_3@BSA-Fe_3O_4 shows characteristic peaks of Bi_2S_3@BSA nanoparticles at $2\theta = 23.78°$, 24.5°, 28.30, 31.78°, 38.9°, 45.52°, 52.8°, and 53.60°, corresponding to 130, 310, 211, 221, 041, 002, 351, and 351 hkl, respectively, which matched with the established standard pattern of Bi_2S_3 (JCPDS No.17-0320).[37] In addition to the characteristic peaks of Bi_2S_3, distinct peaks of Fe_3O_4 nanoparticles appeared at $2\theta = 18.39$, 30.44, 35.55, 43.20, 53.80, 57.11, 62.91, and

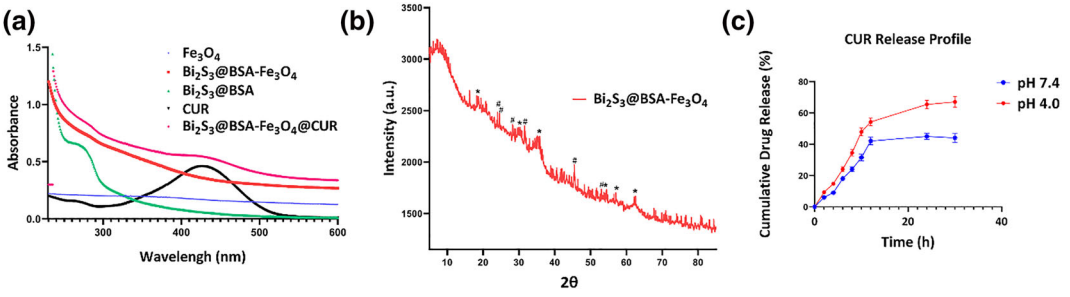

FIGURE 3 (a) UV–Vis spectra of Fe_3O_4, CUR, Bi_2S_3@BSA, Bi_2S_3@BSA-Fe_3O_4, Bi_2S_3@BSA-Fe_3O_4@CUR; (b) XRD pattern of Bi_2S_3@BSA-Fe_3O_4 (# show the characteristic peaks of Bi_2S_3, and * show the characteristic peaks of Fe_3O_4); (c) Release profile of CUR from Bi_2S_3@BSA-Fe_3O_4@CUR

75.25, corresponding to 111, 220, 311, 400, 422, 511, and 440 hkl, respectively. Positions of the peaks conform with the diffraction spectra established for Fe_3O_4 (JCPDS NO.99-100-2343).[38] Furthermore, Bi_2S_3@BSA-Fe_3O_4 hybrid showed a wide peak at 2θ~ 20°, which belongs to BSA on the surface of nanoparticles.[39] Moreover, the NPs show magnetic saturation (MS) about 2.8 emu g^{-1}.

UV–Vis spectrophotometer was used to the estimation of drug-loading efficiency. The DL (%) was found to be 19.8%. The release study of the CUR was investigated in PBS:ethanol (65:35) buffer.[40–42] There is a controlled release pattern for release of CUR from Bi_2S_3@BSA-Fe_3O_4@CUR. Also, the release was higher in pH 4 (<PI) than pH 7.4. As demonstrated in Figure 3c, in an acidic medium (pH 4), about 67% of CUR was released, but under physiological pH (pH 7.4), about 40% of CUR was released. This result is match with Sadeghi et al. study which show that CUR loaded BSA NPs exhibits a maximum release of around 70%.[41]

3.3 | Relaxivity analysis of Bi_2S_3@BSA-Fe_3O_4 as MRI contrast agent

There is an urgency for a safe MRI contrast agent to be used in clinical imaging which can enhance negative and positive contrast synergistically. Thus, fabrication of MRI contrast agents can help with accurate and early diagnosis of cancer. This study was aimed to evaluate T_1 and T_2-weighted contrast potential agent of Bi_2S_3@BSA-Fe_3O_4 nanoparticles. Notably, r_2/r_1 was used as a key parameter to distinguish T_1 and T_2 contrast enhancement of an agent. T_2 contrast agents have higher r_2 and large r_2/r_1 ratio, while T_1 contrast agents should possess high r_1 and smaller r_2/r_1, ideally close to 1.[43]

The ability of synthetized nanohybrid to function as an MRI contrast agent, phantom MRI tests was utilized to evaluate the detectability of the formulated nanohybrid and its sensitivity as a contrast agent. Relaxation times ($r_1 = 1/T_1$ and $r_2 = 1/T_2$) values of all prepared MRI phantoms were calculated and presented as a function of nanohybrid contrast agent concentration (measured in Fe mM) in which T_1 (longitudinal relaxation time) and T_2 (transverse relaxation time) reduce linearly when Fe concentration increases in phantoms, compared with the control phantom. R_1 and R_2 (relaxation rate, or $1/T_1$ and $1/T_2$) had an ascending linear trend with increasing nanohybrid concentration. T_1-weighted images presented in Figure 4a show increasing brightness with increasing nanoparticle concentration, whereas increasing the concentration leads to decreased brightness of T_2-weighted MRI images in Figure 4b. It can be inferred that nanoparticles display both T_1 and T_2 effect.

Further evaluation of a single contrast agent can be evaluated by r_2/r_1 ratio, comparing the effectiveness of T_1 and T_2 contrast mechanisms. Longitudinal (r_1) and transverse molar relaxivity (r_2) were calculated as 1.39 mM^{-1} s^{-1} and 54.73 mM^{-1} s^{-1}, respectively. More

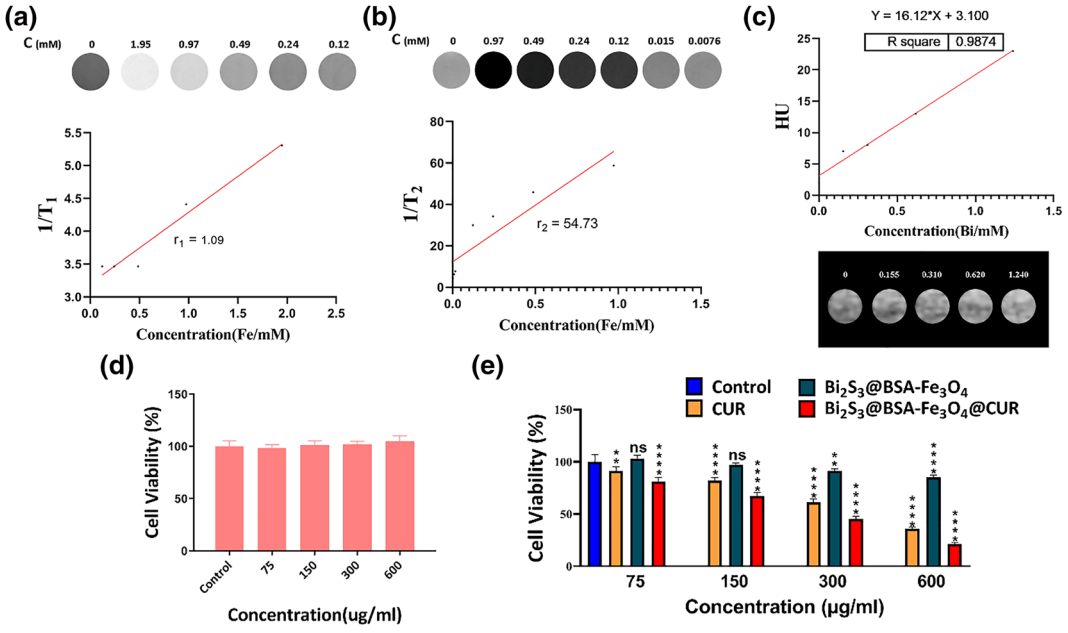

FIGURE 4 (a) T_1-weighted MR images and r_1 relaxivity, (b) T_2-weighted MR images and r_2 relaxivity of Bi_2S_3@BSA-Fe_3O_4, (c) CT contrast effect of the nanohybrid particles at various concentrations; cell viability of (d) HUVEC and (e) 4T1 cells after treatment with nanohybrid particles for 24 h incubation time

importantly, as the synthesized contrast agent shortens both longitudinal and transverse relaxation times, r_2/r_1 (molar relaxivities ratio) is calculated to define the dominant contrast feature of the agent and its efficacy of enhancing image contrast. Accordingly, r_2/r_1 was calculated as 31.83, which demonstrates that nanohybrid displays more negative contrast enhancement than that of positive in MRI.

In an earlier study, for spherical superparamagnetic iron oxide nanoparticles with a diameter of 14 nm, r_2 was reported as 40 mM^{-1} s^{-1}, and these particles were considered as a synergistic contrast agent in vitro.[34] Although the synthetized bimetallic contrast agent can be utilized to achieve T_2-weighted MR images, T_1-weighted phantoms exhibit an acceptable brightness increase in contrast to the control. Our experiments validate previous results and are consistent with the reports that iron oxide nanoparticles show mainly T_2-contrast effect.[44]

3.4 | CT contrast ability of Bi_2S_3@BSA-Fe_3O_4

CT images of Bi_2S_3@BSA-Fe_3O_4 in different concentrations (1.240, 0.620, 0.310, and 0.155 mM of Bi) and deionized water as control sample were collected, and the images were analyzed based on the signal intensity, using macro imaging software. By increasing the nanohybrid concentration (mM of Bi), signal intensity and image brightness increased (Figure 4c). Additionally, HU (CT value, Hounsfield units) increased linearly with elevating nanohybrid concentration (mM of Bi). Earlier, special X-ray attenuation characteristics of Bi-DTPA were reported to be a desirable feature for disease diagnosis in comparison with iopromide (clinical CT contrast agent).[45] Bismuth-based materials are used as an alternative for iodine-based compounds because of the known side effects.[46,47] CT provides high spatial resolution, and its integration with MRI is greatly valuable as more precise complementary information about tumor location could be provided. Nanoparticles offer an opportunity for the integration of MRI contrast agents with high atomic number metals toward enhanced CT imaging. Although our results show that Bi_2S_3@BSA-Fe_3O_4 nanoparticles can act as dual CT/MRI contrast agent, MRI contrast is more important than CT contrast, due to the fact that MRI is more sensitive to soft tissue tumors.

Wang et al. combined iron oxide nanoparticles (T_1-weighted contrast agent) with gold nanocages (as a CT contrast agent) for dual MRI/CT imaging, and the nanoparticles were injected into tumor bearing mice, where combination of both contrast effects in a single probe was reported to be efficient.[48] Our MRI results correlate satisfactorily well with Ma et al.[49] and further support the concept of dual mode imaging to provide accurate diagnosis and elimination of the drawbacks of a single imaging modality. Thus, it implies magnetite/bismuth nanohybrid particles demonstrate excellent behavior as a CT contrast agent.

3.5 | Cytotoxicity studies

The cytotoxicity of Bi_2S_3@BSA-Fe_3O_4 nanoparticles was initially tested by co-incubating HUVEC cells with various doses of nanoparticles for 24 h in order to assess the biocompatibility. The MTT assay was used to evaluate the viability of the cells. For the concentration of nanoparticles in the range of 75–600 μg ml^{-1}, cell viability was always more than 90%, compared with the control group (Figure 4d). Therefore, there was no significant cytotoxicity impact of the nanoparticles on HUVEC cells at treated doses.

Furthermore, the anticancer ability of Bi_2S_3@BSA-Fe_3O_4@CUR nanoparticles was compared with CUR. MTT assay on 4T1 breast cancer cells was used to comparing of anticancer ability. Result show that CUR and Bi_2S_3@BSA-Fe_3O_4@CUR nanoparticles have concentration dependent cytotoxicity. As shown in Figure 4e, cytotoxicity of CUR and Bi_2S_3@BSA-Fe_3O_4@CUR nanoparticles were increased with increasing of concentration of CUR. However, in the same concentration, the Bi_2S_3@BSA-Fe_3O_4@CUR nanoparticles show higher cell proliferation inhibition ability than CUR.

4 | CONCLUSION

Bi_2S_3@BSA-Fe_3O_4 nanohybrid contrast agents possessing X-ray and magnetic contrast properties were prepared via a green synthesis route. The nanohybrid of Fe and Bi provides promising effect on MRI and CT contrast enhancement, superior to conventional iodine-based contrast agents. In vitro MRI relaxivity of as-synthetized nanohybrid revealed T_2-weighted contrast enhancement properties. This study serves as an important step in developing a nanoparticle, which can function both as MRI and CT contrast agent, maximizing the benefits of both imaging modalities. The designed hybrid system was also used as a vehicle for CUR delivery. Bi_2S_3@BSA-Fe_3O_4@CUR nanohybrids not only showed pH sensitivity and controlled release behavior but also offered antiproliferative ability against 4T1 cancer cells.

ACKNOWLEDGMENTS

This work was supported by the Iran National Science Foundation: INSF-98024375, Iran's National Elites Foundation, and the University of Zanjan. We gratefully acknowledge the Zanjan University of Medical Science support. Y.N. Ertas acknowledges funding support from the 2232 International Fellowship for Outstanding Researchers Program of TÜBİTAK (Project No: 118C346).

AUTHOR CONTRIBUTIONS

Hamed Nosrati: Conceptualization; formal analysis; investigation. **Marziyeh Salehiabar:** Investigation; methodology; software. **Faezeh Mozafari:** Software. **Jalil Charmi:** Investigation. **Nuri Erdoğan:** Methodology. **Mohammadreza Ghaffarlou:** Formal analysis; investigation. **Fatemeh Abhari:** Data curation; methodology. **hossein danafar:** Resources; supervision. **Ali Ramazani:** Supervision; validation. **Yavuz Nuri Ertas:** Methodology; resources.

ETHICS STATEMENT

This study was approved by the Ethics Committee of the Iran National Science Foundation, and the study participants signed an informed consent.

DATA AVAILABILITY STATEMENT

The raw/processed data required to reproduce these findings cannot be shared at this time as the data also forms part of an ongoing study.

ORCID

Hamed Nosrati https://orcid.org/0000-0002-7487-8188
Marziyeh Salehiabar https://orcid.org/0000-0003-3881-6358
Faezeh Mozafari https://orcid.org/0000-0002-2866-8817
Jalil Charmi https://orcid.org/0000-0003-2612-8152
Nuri Erdoğan https://orcid.org/0000-0002-3739-933X
Mohammadreza Ghaffarlou https://orcid.org/0000-0003-4833-8118
Fatemeh Abhari https://orcid.org/0000-0002-4504-2998
Hossein Danafar https://orcid.org/0000-0001-8956-7895
Ali Ramazani https://orcid.org/0000-0003-3072-7924
Yavuz Nuri Ertas https://orcid.org/0000-0002-6791-7484

REFERENCES

[1] S. Tang, L. Wei, Y. Sun, F. Zhou, S. Zhu, R. Yang, Y. Huang, H. Zhang, H. Xu, J. Yang, *PLoS ONE* **2016**, *11*(9), e0163030.
[2] Z. He, Z. Chen, M. Tan, S. Elingarami, Y. Liu, T. Li, Y. Deng, N. He, S. Li, J. Fu, W. Li, *Cell Proliferation.* **2020**, *53*(7), e12822.
[3] X. Hou, X. Wang, R. Liu, H. Zhang, X. Liu, Y. Zhang, *RSC Adv.* **2017**, *7*(31), 18844.
[4] A. Datir, S. James, K. Ali, J. Lee, M. Ahmad, A. Saifuddin, *Clin. Radiol.* **2008**, *63*(4), 373.
[5] G. Wright, *IEEE Signal Process. Mag.* **1997**, *14*, 56.
[6] T. Xiao, S. Wen, H. Wang, H. Liu, M. Shen, J. Zhao, G. Zhang, X. Shi, *J. Mater. Chem. B* **2013**, *1*(21), 2773.
[7] N. Lee, S. H. Choi, T. Hyeon, *Adv. Mater.* **2013**, *25*(19), 2641.
[8] N. Lee, T. Hyeon, *Chem. Soc. Rev.* **2012**, *41*(7), 2575.
[9] Y. K. Peng, S. C. E. Tsang, P. T. Chou, *Mater. Today* **2016**, *19*(6), 336.
[10] H. Hu, Y. F. Zhang, S. Shukla, Y. N. Gu, X. Yu, N. F. Steinmetz, *ACS Nano* **2017**, *11*(9), 9249.
[11] T.-H. Shin, Y. Choi, S. Kim, J. Cheon, *Chem. Soc. Rev.* **2015**, *44*(14), 4501.
[12] H. Nosrati, M. Salehiabar, M. Fridoni, M.-A. Abdollahifar, H. K. Manjili, S. Davaran, *Sci. Rep.* **2019**, *9*(1), 1.
[13] Y. N. Ertas, N. N. Jarenwattananon, L. S. Bouchard, *Chem. Mater.* **2015**, *27*(15), 5371.
[14] L. Gu, R. H. Fang, M. J. Sailor, J.-H. Park, *ACS Nano* **2012**, *6*(6), 4947.
[15] L. Hua, Z. Wang, L. Zhao, H. Mao, G. Wang, K. Zhang, X. Liu, D. Wu, Y. Zheng, J. Lu, R. Yu, H. Liu, *Theranostics.* **2018**, *8*(18), 5088.
[16] M. Jeon, M. V. Halbert, Z. R. Stephen, M. Q. Zhang, *Adv. Mater.* **2021**, *33*(23), 1906539.
[17] A. Frtus, B. Smolkova, M. Uzhytchak, M. Lunova, M. Jirsa, S. Kubinova, et al., *J. Controlled Release* **2020**, *328*, 59.
[18] R. Canese, F. Vurro, P. Marzola, *Nanomaterials-Basel.* **2021**, *11*(8).
[19] G. Kandasamy, D. Maity, *Int. J. Pharm.* **2015**, *496*(2), 191.
[20] F. He, H. Ji, L. Feng, Z. Wang, Q. Sun, C. Zhong, D. Yang, S. Gai, P. Yang, J. Lin, *Biomaterials* **2021**, *264*, 120453.
[21] Y. Lu, L. H. Li, Z. F. Lin, M. Li, X. M. Hu, Y. Zhang, M. Peng, H. Xia, G. Han, *Adv. Healthcare Mater.* **2018**, *7*(19), 1800602.
[22] A. L. Brown, A. M. Goforth, *Chem. Mater.* **2012**, *24*(9), 1599.
[23] A. Detappe, E. Thomas, M. W. Tibbitt, S. Kunjachan, O. Zavidij, N. Parnandi, E. Reznichenko, F. Lux, O. Tillement, R. Berbeco, *Nano Lett.* **2017**, *17*(3), 1733.
[24] X.-D. Zhang, J. Chen, Y. Min, G. B. Park, X. Shen, S.-S. Song, Y. M. Sun, H. Wang, W. Long, J. Xie, K. Gao, L. Zhang, S. Fan, F. Fan, U. Jeong, *Adv. Funct. Mater.* **2014**, *24*(12), 1718.
[25] F. Du, J. Lou, R. Jiang, Z. Fang, X. Zhao, Y. Niu, et al., *Int. J. Nanomed.* **2017**, *12*, 5973.
[26] R. A, Y. Yao, X. Guo, W. Jiang, M. Jiang, J. Yang, et al., *ACS Appl. Mater. Interfaces* **2021**, *13*(16), 18604.
[27] S. Xu, J. Wang, Y. Wei, H. Zhao, T. Tao, H. Wang, Z. Wang, J. du, H. Wang, J. Qian, K. Ma, J. Wang, *ACS Appl. Mater. Interfaces* **2020**, *12*(51), 56701.
[28] Y.-T. Wu, C. Shanmugam, W.-B. Tseng, M.-M. Hiseh, W.-L. Tseng, *Nanoscale* **2016**, *8*(21), 11210.
[29] J. Xie, Y. Zheng, J. Y. Ying, *J. am. Chem. Soc.* **2009**, *131*(3), 888.
[30] F. Abhari, J. Charmi, H. Rezaeejam, Z. Karimimoghaddam, H. Nosrati, H. Danafar, A. Farajollahi, *ACS Sustainable Chem. Eng.* **2020**, *8*(13), 5260.
[31] H. Wei, O. T. Bruns, M. G. Kaul, E. C. Hansen, M. Barch, A. Wiśniowska, O. Chen, Y. Chen, N. Li, S. Okada, J. M. Cordero, M. Heine, C. T. Farrar, D. M. Montana, G. Adam, H. Ittrich,

A. Jasanoff, P. Nielsen, M. G. Bawendi, *Proceedings of the National Academy of Sciences.* **2017**, *114*(9), 2325.

[32] C. Tao, Q. Zheng, L. An, M. He, J. Lin, Q. Tian, S. Yang, *Nanomaterials* **2019**, *9*(2), 170.

[33] Y. Wang, Y. Wu, Y. Liu, J. Shen, L. Lv, L. Li, L. Yang, J. Zeng, Y. Wang, L. W. Zhang, Z. Li, M. Gao, Z. Chai, *Adv. Funct. Mater.* **2016**, *26*(29), 5335.

[34] A. Alipour, Z. Soran-Erdem, M. Utkur, V. K. Sharma, O. Algin, E. U. Saritas, H. V. Demir, *Magnetic Resonance Imaging.* **2018**, *49*, 16.

[35] C.-H. Chuang, W.-Y. Chen, W.-B. Tseng, A. Lin, C.-Y. Lu, W.-L. Tseng, *ACS Sustainable Chem. Eng.* **2022**, *10*(7), 2461.

[36] H. Nosrati, E. Attari, F. Abhari, M. Barsbay, M. Ghaffarlou, N. Mousazadeh, R. Vaezi, T. Kavetskyy, H. Rezaeejam, T. J. Webster, B. Johari, H. Danafar, *Bioactive Materials.* **2022**, *7*, 74.

[37] J. Wang, C. Zhou, X. Yan, Q. Wang, D. Sha, J. Pan, et al., *J. Mater. Sci.: Mater. Electron.* **2019**, *30*(7), 6633.

[38] L. Zhuang, W. Zhang, Y. Zhao, H. Shen, H. Lin, J. Liang, *Sci. Rep.* **2015**, *5*(1), 9320.

[39] P. Yang, Q. Liu, J. Liu, H. Zhang, Z. Li, R. Li, L. Liu, J. Wang, *Ind. Eng. Chem. Res.* **2017**, *56*, 3588.

[40] A. V. Samrot, U. Burman, S. A. Philip, N. Shobana, K. Chandrasekaran, *Inform. Med. Unlocked.* **2018**, *10*, 159.

[41] R. Sadeghi, A. Moosavi-Movahedi, Z. Emam-Jomeh, A. Kalbasi, S. Razavi, M. Karimi, et al., *J. Nanopart. Res.* **2014**, *16*(9), 2565.

[42] L. Deng, X. Kang, Y. Liu, F. Feng, H. Zhang, *Food Chem.* **2017**, *231*, 70.

[43] Y.-K. Peng, S. C. E. Tsang, P.-T. Chou, *Mater. Today* **2016**, *19*(6), 336.

[44] Y. Bao, J. A. Sherwood, Z. Sun, *J. Mater. Chem. C* **2018**, *6*(6), 1280.

[45] W. Liao, P. Lei, J. Pan, C. Zhang, X. Sun, X. Zhang, C. Yu, S. K. Sun, *Biomaterials* **2019**, *203*, 1.

[46] K. M. Hasebroock, N. J. Serkova, *Expert Opin. Drug Metab. Toxicol.* **2009**, *5*(4), 403.

[47] A. Tarighatnia, M. R. Fouladi, M. R. Tohidkia, G. Johal, N. D. Nader, A. Aghanejad, H. Ghadiri, *J. Drug Deliv. Sci. Technol.* **2021**, *66*, 102895.

[48] G. Wang, W. Gao, X. Zhang, X. Mei, *Sci. Rep.* **2016**, *6*(1), 28258.

[49] S. Ma, J. Xie, L. Wang, Z. Zhou, X. Luo, J. Yan, G. Ran, *ACS Appl. Mater. Interfaces* **2021**, *13*(9), 10728.

How to cite this article: H. Nosrati, M. Salehiabar, F. Mozafari, J. Charmi, N. Erdoğan, M. Ghaffarlou, F. Abhari, H. Danafar, A. Ramazani, Y. Nuri Ertas, *Appl Organomet Chem* **2022**, e6861. https://doi.org/10.1002/aoc.6861